ACS APPLIED MATERIALS & INTERFACES

Research Article

www.acsami.org

FRET-Based Dual-Emission and pH-Responsive Nanocarriers for Enhanced Delivery of Protein Across Intestinal Epithelial Cell Barrier

Kun-Ying Lu,[†] Cheng-Wei Lin,[‡,§] Chun-Hua Hsu,[∥] Yi-Cheng Ho,[⊥] Er-Yuan Chuang,[⊗] Hsing-Wen Sung,*[,⊗,#,¶] and Fwu-Long Mi*[,‡,§,¶]

[†]Institute of Organic and Polymeric Materials, National Taipei University of Technology, Taipei 10608, Taiwan, ROC

[‡]Department of Biochemistry and Molecular Cell Biology, School of Medicine, College of Medicine and [§]Graduate Institute of Medical Sciences, College of Medicine, Taipei Medical University, Taipei City 11031, Taiwan, ROC

[∥]Department of Agricultural Chemistry, National Taiwan University, Taipei 10617, Taiwan, ROC

[⊥]Department of Bioagriculture Science, National Chiayi University, Chiayi 60004, Taiwan, ROC

[⊗]Department of Chemical Engineering and [#]Institute of Biomedical Engineering, National Tsing Hua University, Hsinchu 30013, Taiwan, ROC

ABSTRACT: The oral route is a convenient and commonly employed way for drug delivery. However, therapeutic proteins have poor bioavailability upon oral administration due to the impermeable barrier from intestinal epithelial tight junction (TJ). Moreover, the pH of the small intestine varies among different regions of the intestinal tract where digestion and absorption occur at different levels. In this study, a tunable dual-emitting and pH-responsive nanocarrier that can alter the fluorescent color and emission intensity in response to pH changes and can trigger the opening of intestinal epithelial TJ at different levels were developed from chitosan-*N*-arginine and poly(γ-glutamic acid)−taurine conjugates. As pH increased from 6.0 to 8.0, the binding affinity of the oppositely charged polyions decreased, whereas the ratio of the intensity of the donor-to-acceptor emission intensity (ID/IA) increased by 27-fold. The fluorescent and pH-responsive nanocarrier was able to monitor the pH change of intestinal environment and to control the release of an anti-angiogenic protein in response to the pH gradient. The nanocarrier triggered the opening of intestinal epithelial TJ and consequently enhanced the permeation of the released protein through the intestinal epithelial barrier model (Caco-2 cell monolayer) to inhibit tube formation of human umbilical vein endothelial cells.

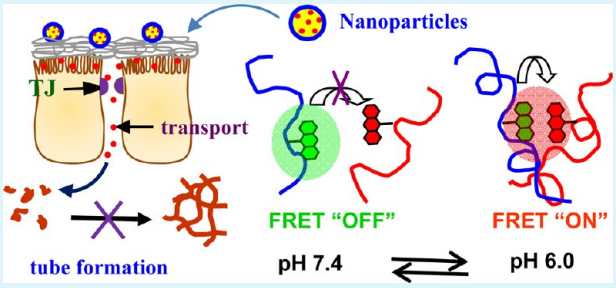

KEYWORDS: *chitosan, pH-responsive, drug delivery, protein release*

INTRODUCTION

Angiogenesis plays a crucial role in a variety of pathological processes, including solid tumor growth and metastasis.[1] The pro-angiogenic factors, such as vascular endothelial and basic fibroblast growth factors (bFGF) and metalloproteinases (MMPs), are associated with tumor progression and transformation.[2] Therefore, inhibition of angiogenesis has grown to be a potential therapeutic target to inhibit tumor growth and metastasis.[3] Recently, nanotechnology-based delivery systems have gained increasing attention in the treatment of cancer.[4−8] Nanocarriers can be made from polymers, lipids, dendrimers, and silica.[9−13] Oral administration of the anti-angiogenic agent such as heparin[14,15] or a low-molecular-weight synthetic analogue of fumagillin, TNP-470,[16,17] using nanosized micelles as drug delivery carriers demonstrated effective anti-angiogenic and anticancer activity. A water-soluble protein derived from shark cartilage has been proved to possess anti-angiogenic and anti-metastatic activity.[18] The angiogenic protein selectively inhibits MMPs and prevents the binding of vascular endothelial growth factor (VEGF) to its receptor, significantly inhibiting angiogenesis.[19,20] Unfortunately, poor oral availability of the anti-angiogenic protein results in failure of effective cancer therapies.[21] Hence, vehicles that can protect the loaded protein from destruction in the gastrointestinal (GI) tract and enhance their intestinal absorption are desperately needed.

Stimuli-responsive nanocarriers have attracted considerable attention as smart materials in biomedical applications.[22,23] The nanomaterials can be used not only as drug delivery systems but also as biosensors and bioimaging materials that are able to respond to stimuli including temperature, pH, and light.[24−28] Chitosan (CS) is a polysaccharide that exhibits excellent wound-healing as well as osteoconductive and antibacterial activities.[29] Chitosan and its derivatives possess mucoadhesive properties, and therefore they have been used for protein and gene delivery.[30−32] Moreover, the nanoparticles could transiently and

Received: August 13, 2014
Accepted: September 26, 2014
Published: September 26, 2014

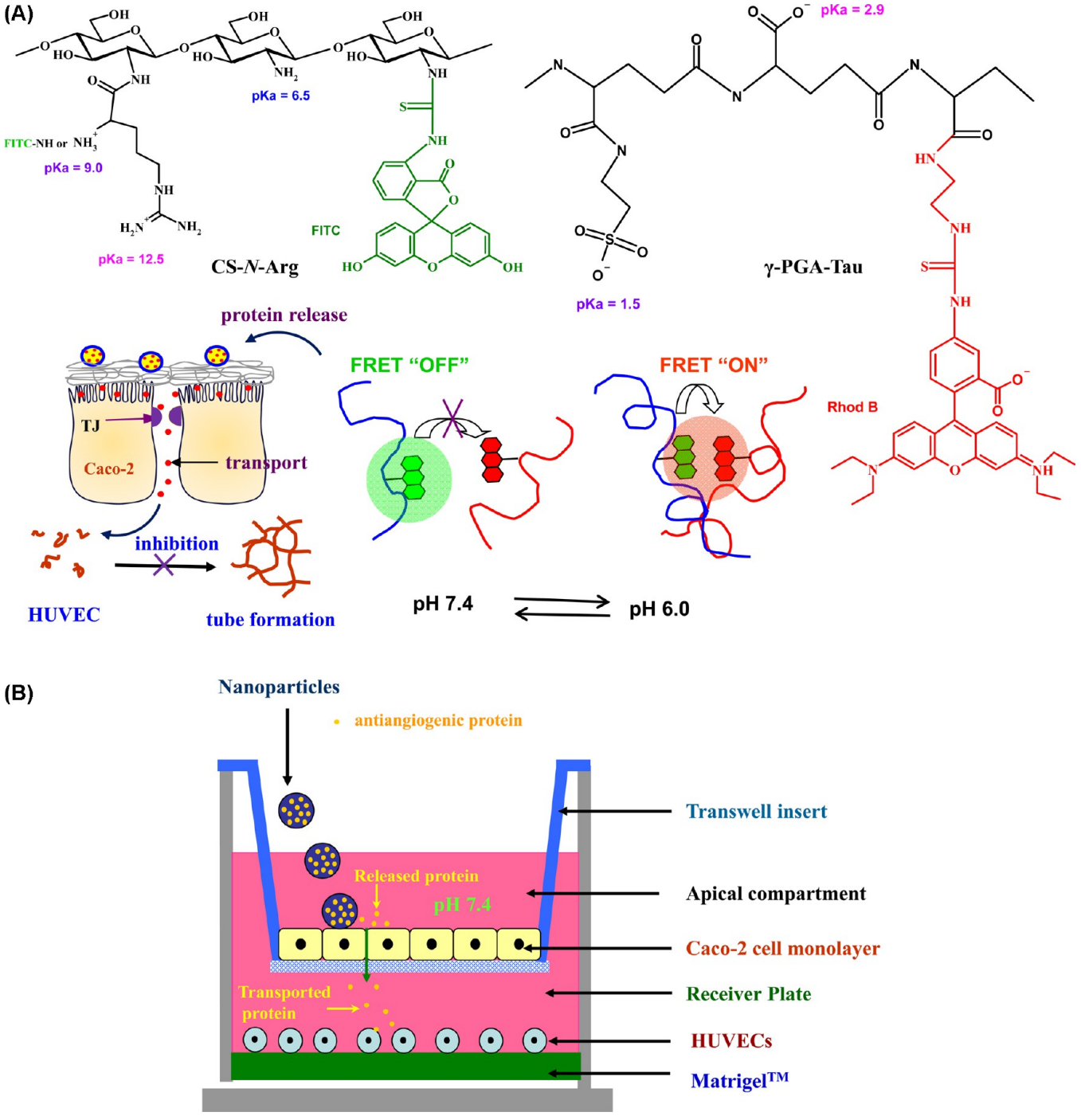

Figure 1. (A) Schematic diagram of experimental design. (B) Schematic diagram displaying the transport of anti-angiogenic protein by adding the protein-loaded nanoparticles in the apical compartment to inhibit HUVEC tube formation in the receiver plate.

reversibly open the tight junctions (TJs) between epithelial cells as chitosan was positively charged.[33]

Our previous study showed the transport of a synthesized, oversulfated fucoidan (OFD) across Caco-2 monolayer by CS-based nanoparticles for anti-angiogenic purpose.[34] However, the CS/OFD nanoparticles became instable at pH higher than 6.0; therefore, the anti-angiogenic activity of transported OFD was not very effective (IC_{50} > 100 μg/mL). Arginine (Arg) is the most basic amino acid containing a guanidine group with a pK_a of 12.5 and a primary amine with a pK_a of 9.0. In this study, grafting of Arg to the nitrogen atom of CS (CS-*N*-Arg conjugate) is supposed to retain more positive charges than CS in a much broader pH, ensuring that the nanoparticles are stable at neutral conditions for opening of tight junction (TJ). Chemical modification of γ-PGA with taurine (Tau) endows the polymer with heparin-like, strong negative charges because Tau contains a sulfonic acid group (p$K_a \approx 1.5$) rather than the carboxylic acid of γ-PGA (p$K_a \approx 2.9$). Moreover, Tau can modulate cellular calcium flux, which is related to TJ opening and paracellular permeability.[35]

Intestinal pH varies slightly among different regions of the intestinal tract where digestion and absorption occur at different levels. This study attempts to develop a Förster resonance energy transfer (FRET)-based fluorescent nanocarrier that is responsive

dx.doi.org/10.1021/am505441p | ACS Appl. Mater. Interfaces 2014, 6, 18275−18289

to the changes in pH of simulated intestinal fluid (SIF). Effects of chemical modification of CS and γ-PGA with Arg and Tau on TJ opening and permeability enhancement of an anti-angiogenic protein in intestinal epithelial cells are also evaluated in Caco-2 cell monolayers. The FRET effect was integrated with the pH-responsive property of the CS-*N*-Arg/γ-PGA-Tau nanoparticles to monitor the pH changes and control the protein release. The nanoparticle triggered the opening of TJ and thereby enhanced the permeation of the anti-angiogenic protein through Caco-2 cell monolayers. Inhibition of tube formation of human umbilical vein endothelial cells (HUVEC) by the permeated protein was also examined. A schematic diagram of experimental design is shown in Figure 1A.

MATERIALS AND METHODS

Materials. Shark cartilage was obtained from a blue shark (*Prionace glauca*) (Grand Ocean Seafoods Co, Ltd., Taiwan). CS (Mw 60 kDa, DDA 0.85) was purchased from Koyo Chemical Company Limited. γ-PGA (Mw 100 kDa) was obtained by VEDAN Enterprise Corporation. Arg, Tau, ethylenediaminetetraacetic acid (EDTA), 1-ethyl-3-(3-(dimethylamino)propyl)-carbodiimide hydrochloride (EDC), *N*-hydroxysuccinimide (NHS), 3-(4,5 dimethylthazol-2-yl)-2,5 diphenyl tetrazole bromide, dimethyl sulfoxide (DMSO), fluorescein isothiocyanate (FITC), and rhodamine B (Rhod B) were obtained from Sigma–Aldrich.

Purification and Characterization of Protein. The anti-angiogenic protein was purified according to the literature procedures.[36] The crude extract of shark cartilage was obtained after homogenization in a Tris-buffered saline (20 mM Tris–HCl, pH 8.0, 100 mM NaCl, and 0.1 mM EDTA) and centrifuged at 14 000 rpm (Beckman JA-20) for 30 min. The solution was concentrated using a Vivaflow-50 (10 kDa cutoff) (Vivascience). The resulting shark crude extract solution (5 mL, 25 mg protein/ml) was applied to a 500 ml Pharmacia XK-50 column packed with Toyopearl HW-50 gel filtration column, and the eluted fractions (10 mL) dialyzed against Tris buffer were pooled and concentrated using a centrifugal filter device (10 kDa cutoff, Vivascience). An aliquot of the purified fraction was analyzed by 12% sodium dodecyl sulfate polyacrylamide gel electrophoresis (SDS-PAGE) (acrylamide/bisacryamide ratio is 29:1).

Synthesis and Characterization of Polymer Conjugates. The solution of Arg activated by NHS/EDC (molar ratio of EDC/NHS/Arg = 4:4:1) was added to the chitosan solution (5 mg/mL, 100 mL), and the resulting mixture was allowed to react for 24 h. The γ-PGA/EDC mixed solution was added with adequate amounts of Tau (molar ratio of γ-PGA/Tau/EDC = 1:1:0.5), and the resulting mixtures were allowed to react for 24 h. The obtained CS-*N*-Arg and γ-PGA-Tau polymer conjugates were purified by dialysis followed by freeze-drying. The purified products were dissolved in D_2O and analyzed by a Bruker Avance 500 MHz nuclear magnetic resonance (NMR) spectrometer at 300 K. Fourier transform infrared spectra (FTIR) of the purified products in KBr pellets were recorded between 4000 and 500 cm^{-1} on a PerkinElmer RX1 FTIR spectrometer. Degrees of substitutions of the synthesized CS-*N*-Arg and γ-PGA-Tau polymer conjugates were characterized by ^1H NMR spectra.

Titration and Polyelectrolyte Complexation. A polycation/polyanion complexation method was used to prepare CS-*N*-Arg/γ-PGA-Tau nanoparticles. Nanoparticle dispersions were prepared by the titration of an aqueous CS-*N*-Arg (1.2 mg/mL, 20 mL) with an aqueous γ-PGA-Tau (2.0 mg/mL) under continuous stirring. Transmittance of nanoparticles dispersions was determined at various γ-PGA-Tau-to-CS-*N*-Arg volume ratios using a Hitachi U-1900 UV–vis spectrophotometer at 500 nm.[37] The average particle sizes and surface charges of nanoparticle dispersions were measured by dynamic light scattering (DLS) using a Malvern 3000HS Zetasizer. The pH values of nanoparticle dispersions were adjusted to pH 2.0, 2.5, 6.0, 6.5, 7.0, and 7.4 to simulate the pH of gastric and intestinal fluids.[40,41]

Isothermal Titration Calorimetry (ITC). The interactions between the oppositely charged polyelectrolytes were determined by Nano ITC (TA Instruments, USA). The CS-*N*-Arg solutions (1.2 mg/mL, 1030 μL) were kept in the sample cell with the reference cell filled with deionized water, while the injector was filled with γ-PGA-Tau solutions (4.0 mg/mL). The γ-PGA-Tau solution was injected in 5 μL aliquots of a 5.0 mg/mL solution into the sample cell under 250 rpm stirring at 298 K. Total amount of the injection was 250 μL. The injected titrant and the samples were kept at 6.0, 6.5, and 7.4. Data acquisition was performed with NanoAnalyze software (TA Instruments) and was shown as a plot of observed enthalpy change per mole of injectant (ΔH_{obs}, kJ mol^{-1}) against molar ratio. Equilibrium binding constants, heats of binding, and stoichiometries were determined by nonlinear least-squares fitting for isothermal titration calorimetry (ITC) data analysis.

FRET and pH-Responsive. FITC-labeled CS-*N*-Arg and Rhod B-labeled γ-PGA-Tau was synthesized by the following process. Briefly, FITC was dissolved completely in DMSO (0.2 mg/mL). Afterward, 1 mL of the FITC solution was subsequently added to 50 mL of CS-*N*-Arg solution (5 mg/mL). Rhod B-labeled γ-PGA-Tau was synthesized by activating the carboxyl groups of γ-PGA-Tau (20 mL, 5 mg/mL) with 0.05 g of EDC/0.025 g of NHS mixture at pH 6.0 for 1 h. Rhod B (0.012 g) and ethylenediamine (2 μL, 99.5%) were dissolved in 10 mL of ethanol. The Rhod B/ethylenediamine mixture was subsequently added to the activated γ-PGA-Tau solution. After 12 h of reaction, the FITC-labeled CS-*N*-Arg and Rhod B-labeled γ-PGA-Tau were dialyzed to completely remove the residual dyes. The lyophilized fluorescent products were used to prepare nanoparticles according to the aforementioned method.

FRET spectra of the FITC-labeled CS-*N*-Arg/Rhod B-labeled γ-PGA-Tau systems were measured by a PerkinElmer EnSpire 2300 multimode plate reader via the excitation of the donor (FITC) at 488 nm and the recording of the emission spectra of the donor (FITC, 520 nm)/acceptor (Rhod B, 585 nm) pairs. Assembly of the CS-*N*-Arg/γ-PGA-Tau nanocomplex was investigated by a titration study, and the FRET spectra were recorded. An amount of Rhod B-labeled γ-PGA-Tau (0–500 μL, 2 mg/mL) was added to 1 mL of FITC-labeled CS-*N*-Arg (1.2 mg/mL), and the emission spectrum was recorded to determine the ratio of the donor-to-acceptor emission intensity (ID/IA). The dissociation of the CS-*N*-Arg (1.2 mg/mL, 1 mL)/γ-PGA-Tau (2 mg/mL, 500 μL) nanocomplex was examined by keeping the nanocomplexes (500 μL of Rhod B-labeled γ-PGA-Tau) at distinct pH values, and the FRET spectrum was recorded. The formation and dissociation of CS-*N*-Arg/γ-PGA-Tau nanocomplexes were also visualized using a confocal laser scanning microscopy (CLSM, Leica TCS SP2). The nanocomplexes (200 μg/mL) were mixed with an equal volume of agar (5 wt %) at 65 °C. Afterward, a 20 μL tip was immediately dipped into the nanocomplex/agar mixed gel suspension to transfer the gel suspension onto a microscope slide. The slide was excited by 488 nm laser light, and then imaged with emission filters for

sequential visualization of green (520 ± 10 nm) and red (580 ± 10 nm) emission.

Protein Loading and Release. Stock solution of anti-angiogenic protein was premixed with an aqueous γ-PGA-Tau to obtain an anti-angiogenic protein (1.5 mg/mL)/γ-PGA-Tau (2 mg/mL) solution. Subsequently, the mixed solution (3.5 mL) was added to the CS-*N*-Arg solution (1.2 mg/mL, 10 mL) according to the previously described procedure. After centrifuging nanoparticles from the dispersions, the supernatant was assayed by Bradford protein assay kit (Bio-Rad Protein Dye Reagent; Bio-Rad) at λ_{max} 595 nm to measure the amount of loaded anti-angiogenic protein. Furthermore, the protein was labeled with FITC for fluorescence examination. FITC was dissolved completely in DMSO (0.2 mg/mL). Afterward, 0.5 mL of the FITC solution was subsequently added into 10 mL of protein solution (5 mg/mL). After 12 h of reaction, the FITC-labeled protein was dialyzed to remove the residual dyes. The FITC-labeled protein was incorporated in the γ-PGA-Tau/CS-Arg nanoparticles according to the above-mentioned procedure. After removal of the supernatant, the nanoparticles were resuspended in 5 mL of deionized water and subsequently recentrifuged. The fluorescene intensity was measured using a PerkinElmer EnSpire 2300 multimode plate reader by exciting the sample at 488 nm and recording the emission at 520 nm.

The in vitro release of anti-angiogenic protein from test nanoparticles was determined by placing the anti-angiogenic protein-loaded nanoparticles in buffers of pH 2.5, 6.0, 6.5, 7.0, 7.4, and 8.0 at 37 °C, respectively. At the end of the time period (300 min), 100 μL of samples withdrawn from the release medium were analyzed by the above-mentioned Bradford method to determine the release profile. Time-dependent release was performed by continuously adjusting the pH of release medium (pH 2.5, 120 min; pH 6.5, 120 min; pH 7.0, 120 min; pH 7.4, 360 min) to simulate the gastrointestinal tract conditions.

Cytotoxicity of Nanoparticles on Caco-2 Cells. Caco-2 cells were seeded onto 96-well plates at a density of 3×10^4 cells/well and cultured in Dulbecco's Modified Eagle Medium (DMEM, 200 μL) for 24 h. The protein-free and loaded nanoparticle suspension (2 mg/mL) were diluted (25−500 μg/mL) with culture medium. After 48 h of incubation at 37 °C, MTT (200 μL, 0.5 mg/mL in DMEM) was added to the cells, and the plate was kept in an incubator for 2 h at 37 °C. The supernatant was aspirated, and 100 μL of DMSO was added to dissolve the formazan crystals. The intensity of color was measured on a plate reader (PowerWave X340, Bio-TEK Instrument, Inc., USA) at 570 nm. Cell viability was expressed as percentage of absorbance relative to control.

Transport Properties. Caco-2 cells were cultured and grown into monolayers on polycarbonate membrane transwell inserts (Corning Costar Corp., NY). After three weeks, the tightness of Caco-2 monolayer was evaluated by measurement of transepithelial electrical resistance (TEER larger than 800 Ω cm^2) using a Millipore Millicell-ERS meter after pre-equilibrated with HBSS buffered at different pH values. Subsequently, the nanoparticle solution at a concentration of 0.2 mg/mL was added to the apical compartment, while an aliquot (50 μL) of the medium in the basolateral compartment (pH 7.4) was collected at a predefined interval of time. Changes in TEER were measured using a Millicell-Electrical Resistance System (Millipore Corp., Bedford, MA). The cells were incubated with rabbit anti-ZO-1 monoclonal antibody (Zymed Laboraties) and subsequently stained by a Cy-3 conjugated goat antirabbit IgG (Jackson ImmunoResearch Laboratories). Dislocation of ZO-1 protein in Caco-2 cells was examined under a confocal laser scanning microscopy (CLSM, Leica TCS SP2). Additionally, cells were costained with 5 μg/mL propidium iodide (PI, P4864, Sigma-Aldrich) to visualize nuclei. The transported protein was quantitatively measured by the aforementioned Bradford protein assay. The apparent permeability coefficients (P_{app}) were determined as follows:

$$P_{app}\ (\mathrm{cm/s}) = (\Delta Q/\Delta t)/(A \times C_0)$$

where $\Delta Q/\Delta t$ (μg/s) is the cumulative amount transported, A is the diffusion area (1.12 cm^2), and C_0 is the initial protein concentration in the donor side (μg/mL).

In Vitro Antiangiogenesis Assay. Human umbilical vascular endothelial cell (HUVEC) were seeded in the basolateral compartment coated with Matrigel (BD Biosciences), subsequent to the growth of Caco-2 cell monolayers. At 24 h post seeding, free protein and protein-loaded nanoparticles (5, 10, 25, and 50 μg of protein equivalent/milliliter to the concentration in the basolateral compartment) in HBSS (pH 7.4) were, respectively, added to the apical compartment (insert). Nanoparticles were removed after 2 h of incubation by washing the cell with phosphate-buffered saline (PBS). The HUVEC cells were cultured for an additional 48 h subsequent to the removal of nanoparticles from the insert. The images from a microscope (Nikon, TS100, Japan) were used to measure the tube length. The following formula was used to calculate inhibition rate of tube formation: rate of inhibition (%) = [1-(tube length_{sample}/tube $\mathrm{length}_{control}$)] × 100.[38] The experimental design for the transport of anti-angiogenic protein across the epithelial barrier to inhibit HUVEC tube formation is shown in Figure 1B.

RESULTS AND DISCUSSION

Characterization of CS-N-Arg and γ-PGA-Tau Conjugates. Figure 2A shows the ^{1}H NMR spectra of CS and the CS-*N*-Arg conjugate. CS-*N*-Arg conjugate demonstrated a new signal at 1.52 ppm (methylene band) in addition to those observed at 3.09−3.13 ppm (corresponding to the guanidine bands). Figure 2B exhibits the representative FTIR spectra of CS and the CS-*N*-Arg conjugate. The absorption of guanidine group at 1563 cm^{-1} is observed, while the characteristic carbonyl stretching (C═O) appeared at 1652 cm^{-1} owing to the formation of amide bonding. These results indicated that chitosan was conjugated with arginine. The degree of arginine substitution (DS_{Arg}) of the CS-*N*-Arg conjugate was calculated according to the following formula:

$$\mathrm{DS_{Arg}} = (\text{peak area of protons on position } c \div \text{peak area of protons on } \mathrm{CH_3}) \times (3/2) \times (\text{degree of acetylation of CS})$$

Figure 2C,D shows the spectrochemical analysis of γ-PGA and the γ-PGA-Tau conjugate, respectively. As shown in the ^{1}H NMR spectra (Figure 2C), the characteristic signals of γ-PGA and the CH_2 of Tau (strongly coupled multiplet) were observed after conjugation. The peaks of CH_2 next to nitrogen and sulfur atom were shifted from 3.17 and 3.33 ppm in Tau to 3.01 and 3.51 ppm in γ-PGA-Tau conjugate. The result suggested that γ-PGA was successfully conjugated with Tau. The characteristic absorption bands at 1217 cm^{-1} (O═S═O asymmetric stretch) appeared, while the characteristic peak at 1652 cm^{-1} for carboxyl group decreased in γ-PGA-Tau conjugate owing to the

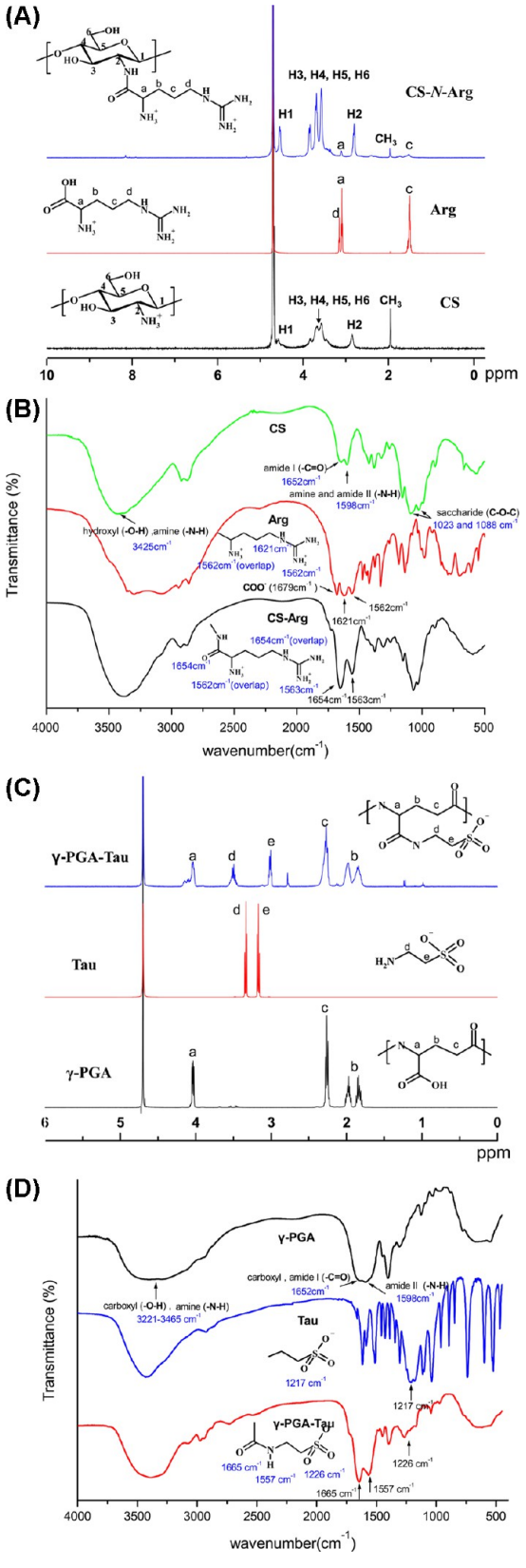

Figure 2. ^{1}H NMR and FTIR spectra of CS-*N*-Arg and γ-PGA-Tau conjugates: (A) ^{1}H NMR spectra of CS, Arg, and CS-*N*-Arg conjugates, (B) FTIR spectra of CS, Arg, and CS-*N*-Arg conjugates, (C) ^{1}H NMR spectra of γ-PGA, Tau, and γ-PGA-Tau conjugates, and (D) FTIR spectra of γ-PGA, Tau, and γ-PGA-Tau conjugates.

introduction of Tau. These results indicated that Tau has been successfully coupled to γ-PGA. Degree of Tau substitution (DS_{Tau}) of the γ-PGA-Tau conjugate was calculated according to the following formula:

$$DS_{Tau} = (\text{peak area of protons on position } d \div \text{peak area of proton on position } a) \times (1/2)$$

where the degree of acetylation of chitosan is 0.15. The DS_{Arg} value estimated from the obtained ^{1}H NMR spectra was 0.13 (13%), while that of DS_{Tau} was 0.29 (29%).

Charge Ratio of CS-*N*-Arg/γ-PGA-Tau Complex. The sharp decrease in transmittance (*T*%) at 500 nm upon adding aqueous γ-PGA (or γ-PGA-Tau) into CS (or CS-*N*-Arg) aqueous solution was an evidence of forming insoluble colloidal dispersions. This was attributed to the formation of self-assembled CS-*N*-Arg/γ-PGA-Tau nanoparticles by mixing the oppositely charged polyelectrolytes. Figure 3A shows the turbidimetric titration curves for the titration of a CS-*N*-Arg (with charged amine A and guanidine G) solution with an aqueous γ-PGA-Tau (with charged carboxylate C and sulfonate S), based on distinct molar ratios (the γ-PGA-Tau/CS-*N*-Arg

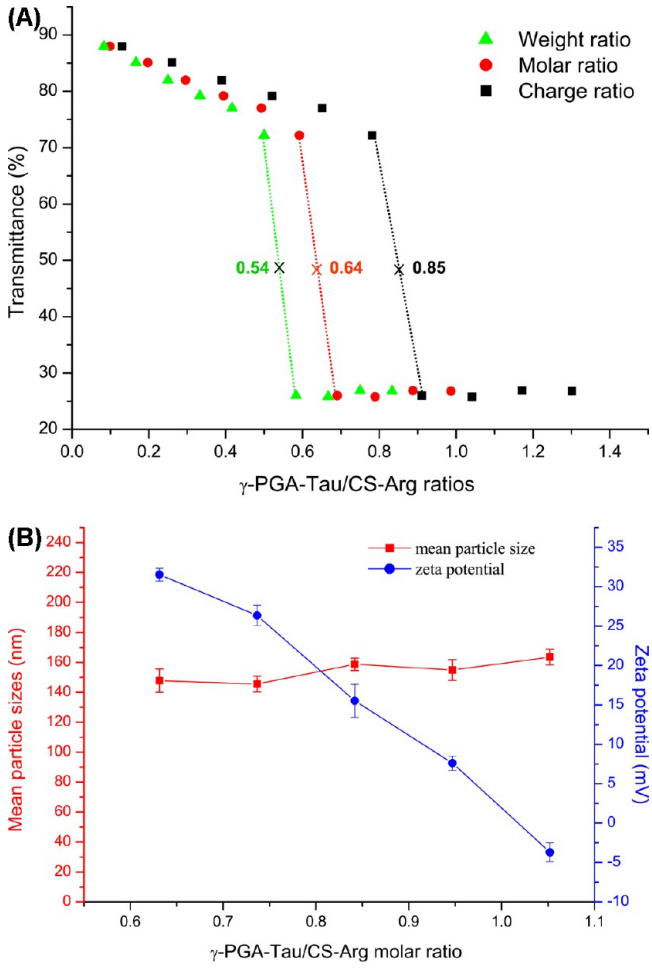

Figure 3. (A) Turbidimetric titration (transmittance) curves for the titration of a CS-*N*-Arg solution (1.2 mg/mL, 2 mL) with an aqueous γ-PGA-Tau (2 mg/mL, 0.1−1 mL) based on distinct weight ratios, molar ratios, and theoretical charge ratios. (B) Average sizes and ζ potentials of γ-PGA-Tau/CS-*N*-Arg colloidal nanocomplex formed at different γ-PGA-Tau to CS-*N*-Arg molar ratios.

dx.doi.org/10.1021/am505441p | ACS Appl. Mater. Interfaces 2014, 6, 18275−18289

molar ratios) and theoretical charge ratios (the (C+S)/(A+G) ratios). The titration curves exhibited a sharp decrease in transmittance at a γ-PGA-Tau-to-CS-*N*-Arg molar ratio of 0.64. Considering of the charges on γ-PGA-Tau and CS-*N*-Arg, the inflection point shifted from 0.64 (molar ratio) to 0.85 (charge ratio). Above the inflection point, the transmittance level decreased sharply to less than 27%, suggesting the formation of well-organized nanoparticles due to strong interactions between CS-*N*-Arg and γ-PGA-Tau. The nanoparticle dispersion was stable without flocculation; even the molar ratio increased to 1.0 (charge ratio increased to 1.3). Nevertheless, turbidity can be affected by several physical properties of nanoparticles, such as light scattering, size, and polydispersity, which can be measured by DLS to monitor the formation of nanoparticle. At molar ratios lower than 0.64, the K-count (kilocounts per second, kcps) of prepared nanoparticle dispersions were low (<30 kcps), indicating a few nanoparticles were produced. The mean particle size and zeta (ζ) potential measured at this condition may be inaccurate. Therefore, Figure 3B only showed the particle size and ζ potential data for the nanoparticles prepared at molar ratios higher than 0.64. The diameters of CS-*N*-Arg/γ-PGA-Tau nanoparticles increased from 148 to 164 nm when molar ratio increased from 0.63 to 1.05 (Figure 3B). However, the ζ potentials determined from the nanoparticles are strongly influenced by the CS-*N*-Arg to γ-PGA-Tau molar ratios of oppositely charged polyelectrolytes. These significant differences were likely related to the excess polyanions (γ-PGA-Tau) or polycations (CS-*N*-Arg) located on the surface, which produced different effective charges of nanoparticles. As shown in Figure 3B, the ζ potential values decreased with the increase of CS-*N*-Arg/γ-PGA-Tau ratios. The ζ potential values became negative when γ-PGA-Tau/CS-*N*-Arg molar ratios increased to higher than 1.0 because the nanoparticles were surrounded by excessive, negatively charged γ-PGA-Tau.

Effect of pH on Charge Ratio. The theoretical charges on polyanions (γ-PGA and γ-PGA-Tau) and polycations (CS and CS-*N*-Arg) were severely affected by the pH value. At pH 6.0, the charge ratios of CS and CS-*N*-Arg were 64.6% and 71.2% as calculated by the Henderson−Hasselbalch equation from the pK_a of guanidine (12.7) and the primary amine, respectively, on chitosan (6.5) and arginine (9.0). However, the charge ratios decreased sharply to 9.5% and 29.1% as pH increased to 7.4. Similarly, the charge ratios of γ-PGA and γ-PGA-Tau decreased from 99.5% and 99.9% to 28.5% and 46.6% as pH decreased from 6.0 to 2.5. The charge ratios even decreased to 11.2% and 30.3% as pH decreased to 2.0. The results reveal that the modification of CS and γ-PGA with Arg and Tau can contribute to retaining the charges on macromolecular chains that increase the stability of prepared nanoparticles over a wide pH range (2.0−7.0). The pH-responsive properties of CS-*N*-Arg/γ-PGA-Tau nanoparticles were evaluated by the variation of polydispersity index (PDI) of the nanoparticles at distinct pH ranges (Table 1). Dissociation of complex coacervation can be described by the indices of increasing PDI of the nanoparticle dispersions. The complexation between oppositely charged CS-*N*-Arg and γ-PGA-Tau was stably retained by increasing pH from 2.5 to 6.5, and the alteration of PDI of nanoparticle dispersions was not obvious (PDI < 0.2). As pH increased to 7.4, the (C+S) /(A+G) ratio increased, and the PDI appreciably increased due to the imbalance of electrostatic attractions.

The permeation of protein across intestinal barriers is a complex process consisting of mucoadhesion, TJ opening, and protein release. Surface charge plays an important role not only in adherence and infiltration of CS-based nanoparticles into the mucus layer but also in the disruption of the epithelial tightness. Increase of the environmental pH will decrease positive charges on the surface of nanoparticles (Table 1). At pH 6.0, the ζ potential of the nanoparticles was 32.9 mV because CS-*N*-Arg conjugates with their polysaccharide backbones filled with protonated amine and guanidinium cation were effectively charged (71.2%). However, raising the pH to 7.4 caused the decrease of electrostatic attraction between the oppositely charged polyelectrolytes because the amino groups on the glucosamine unit became almost deprotonated (only 6.6% remained). However, more primary amine and guanidinium cations on arginine remained (22.5%). The ζ potentials decreased to 17.3 mV due to the deprotonation of amino groups in the CS-*N*-Arg conjugates. Nevertheless, the nanoparticles were still positively charged over the pH range of 2.0−7.4 (Table 1), suggesting that the cationic CS-*N*-Arg conjugates were retained on the surface of CS-*N*-Arg/γ-PGA-Tau nanoparticles.

Table 1. Mean Particle Sizes, Zeta Potential Values, and Polydispersity Indices of CS-*N*-Arg/γ-PGA-Tau NPs at Distinct pH Environments (n = 5 batches)

pH	average size (nm)	ζ potential (mV)	PDI
2.0	275.9 ± 2.9	38.1 ± 2.5	0.32 ± 0.05
2.5	164.7 ± 4.2	36.8 ± 0.6	0.15 ± 0.09
6.0	147.1 ± 3.6	32.9 ± 1.7	0.13 ± 0.04
6.5	160.5 ± 5.2	30.2 ± 2.4	0.12 ± 0.11
7.0	184.4 ± 4.5	23.7 ± 1.1	0.16 ± 0.06
7.4	261.3 ± 5.2	17.3 ± 1.5	0.28 ± 0.07

Calorimetric Evaluation of Nanoparticle Stability. CS has been recognized as a potential permeation enhancer for mucosal drug delivery. However, CS could be deprotonated at pH > 6.5, resulting in a decrease of its TJ opening capability. Its mechanism of TJ disruption is mediated by the positive charge on the protonated CS, although some cationic polymers other than chitosan were not effective in opening the TJs.[39] Moreover, γ-PGA is a macromolecular peptide that consists of glutamic acid and is polymerized by γ-glutamyl bonds. The carboxylate ions in γ-PGA could be protonated in the gastric juice because its pK_a value is ∼2.9, which leads to a breakdown of the self-assembled CS/γ-PGA nanostructure.[30] To overcome these disadvantages, CS was modified with arginine, possessing strong basic guanidinium groups, to retain the positive charges at pH > 6.5, whereas γ-PGA were modified with Tau, possessing strong acidic sulfonate groups, to retain its negative charges at pH < 2.9.

ITC has been used to characterize the thermodynamics of the reaction between two oppositely charged polyelectrolytes. Analysis of the heat changes occurred when γ-PGA-Tau titrated into CS-*N*-Arg solution revealed multiple steps in complexation. Huang et al. proposed a model describing the interaction between oppositely charged polyelectrolytes.[40] This model suggested that the formation of colloidal complex consisted of the process of cooperative binding during ion pairing and subsequent complex coacervation. At the first stage of complexation, the exothermic binding enthalpy increased with the γ-PGA-Tau concentration as pH was kept at 6.0 (Figure 4A). The binding affinity of γ-PGA-Tau/CS-*N*-Arg ion pairs increased as more oppositely charged polyions associated, although the binding sites of CS-*N*-Arg were covered by the oppositely charged γ-PGA-Tau. This result revealed that a cooperative binding occurred at the first stage of complexation.

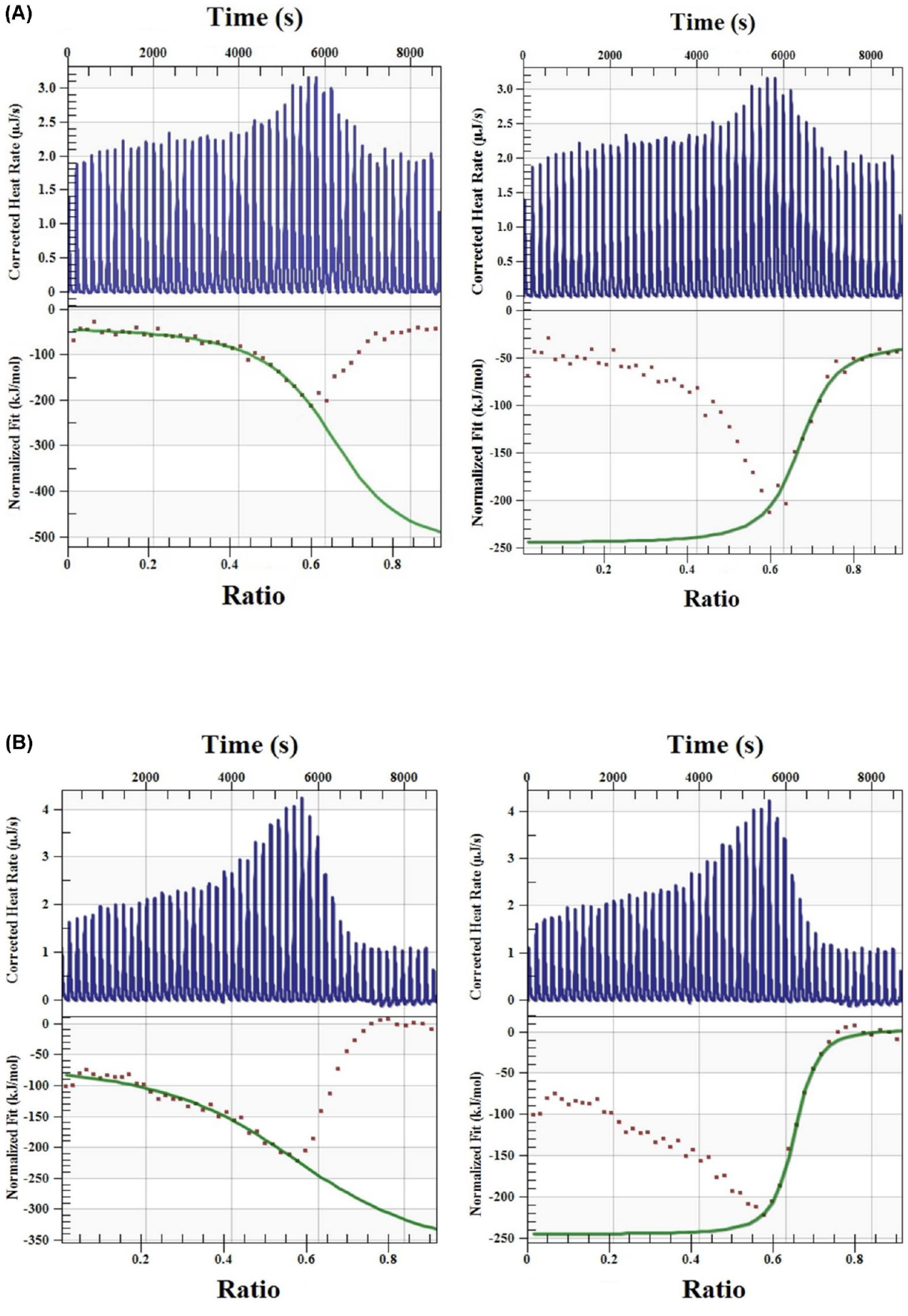

Figure 4. continued

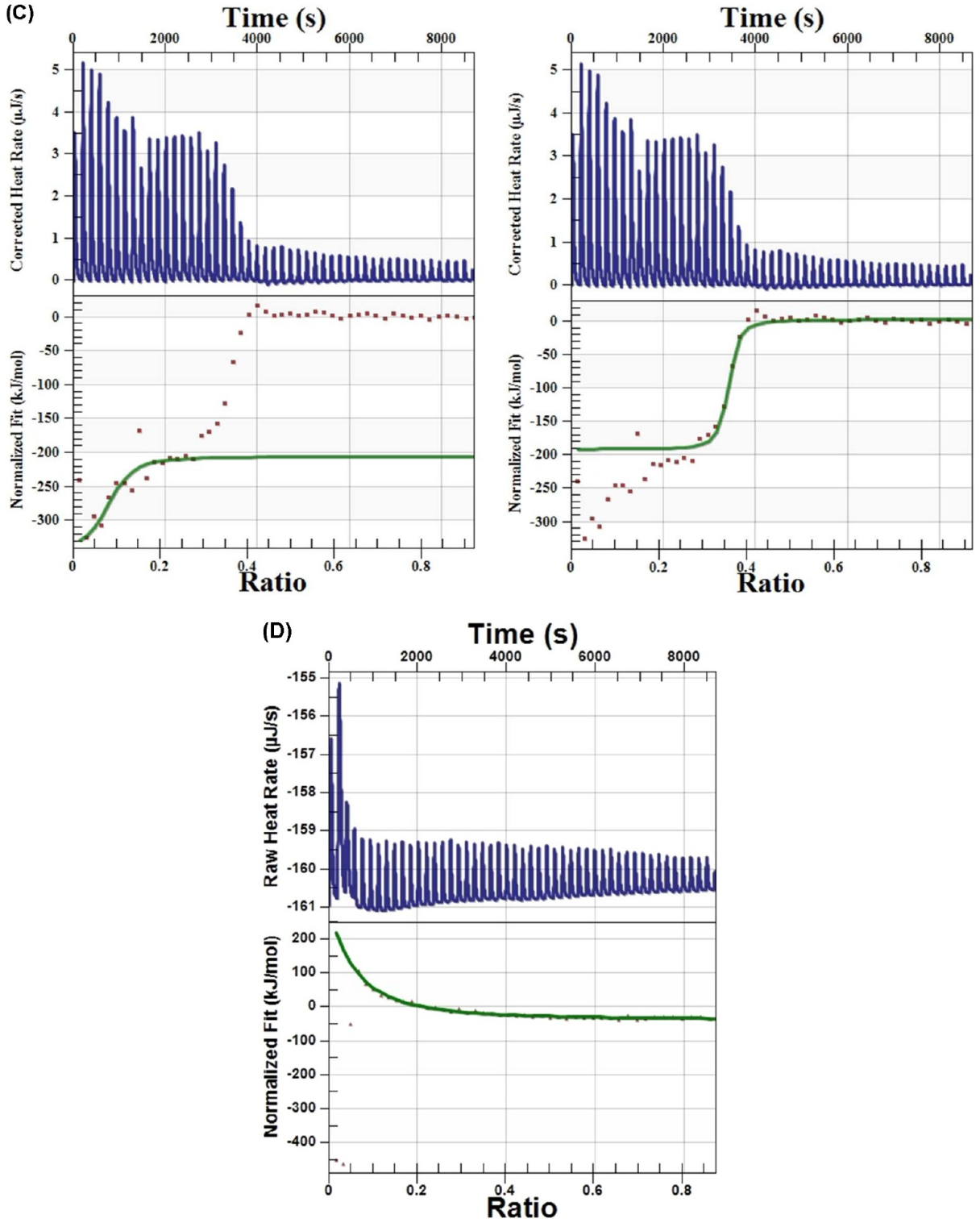

Figure 4. ITC raw data (upper) and corresponding plot after integration of peak areas and normalization (lower). Representative data are shown for the titration of CS-*N*-Arg solution (1.2 mg/mL, 1030 μL) in the reaction cell with γ-PGA-Tau solution (4.0 mg/mL) in 5.0 μL aliquots from the injection syringe. The γ-PGA-Tau solution was injected in 5 μL aliquots of a 4.0 mg/mL solution into the sample cell under 250 rpm stirring at 298 K. Total amount of the injected γ-PGA-Tau was 250 μL. (A–C) Titration of CS-*N*-Arg solution with γ-PGA-Tau solution at (A) pH 6.0, (B) 6.5, and (C) 7,4. (D) Titration of CS solution with γ-PGA solution at pH 7.4.

As the titration approached the above-mentioned inflection point (γ-PGA-Tau/CS-*N*-Arg molar ratio = 0.60–0.65), where the transmittance of the γ-PGA-Tau/CS-*N*-Arg system sharply decreased (Figure 4A), the exothermic binding enthalpy inversely increased to −49 kJ/mol, indicating that the binding sites were saturated as the molar ratio increased to 0.9. The polyelectrolyte complexes formed in the former stage of titration, via the cooperative binding, were subsequently aggregated into coacervates for particles growth. The intersection of cooperative binding (the first stage) and complex coacervation (the second

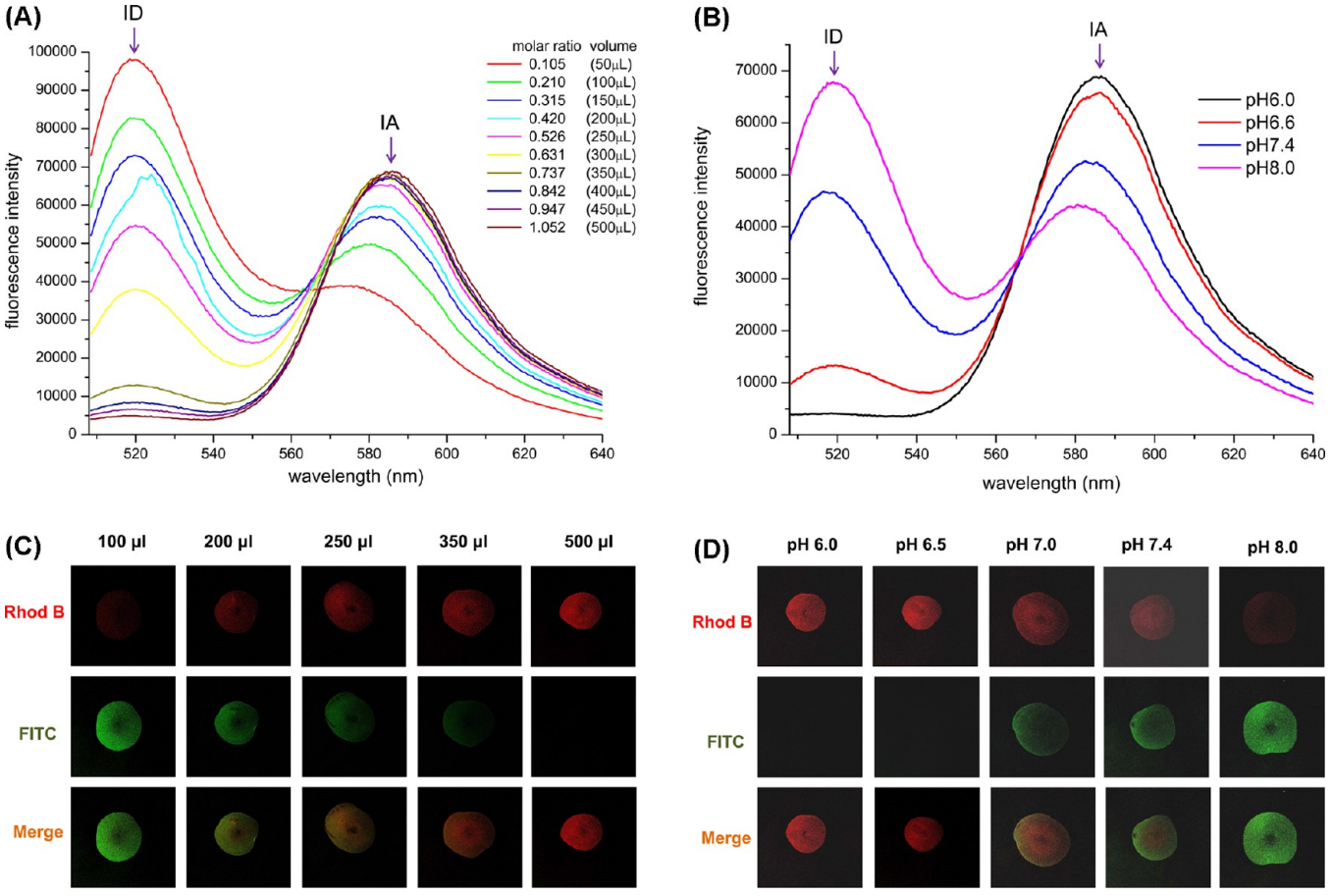

Figure 5. (A) FRET emission spectra of FITC−CS-*N*-Arg/Rhod B-γ-PGA-Tau nanocomplex prepared by the titration of FITC−CS-*N*-Arg (1.2 mg/mL, 1 mL) with aqueous Rhod B-γ-PGA-Tau (2 mg/mL, 0−500 μL). (B) pH-dependent FRET spectra of FITC−CS-*N*-Arg (1.2 mg/mL, 1 mL)/Rhod B-γ-PGA-Tau (2 mg/mL, 500 μL) nanoparticle disperions. (C) FRET imaging of FITC−CS-*N*-Arg/Rhod B-γ-PGA-Tau nanocomplex formed by titration of FITC−CS-*N*-Arg (1.2 mg/mL, 1 mL) with aqueous Rhod B-γ-PGA-Tau (2 mg/mL, 100, 200, 250, 350, and 500 μL). (D) FRET imaging of FITC−CS-*N*-Arg (1.2 mg/mL, 1 mL)/Rhod B-γ-PGA-Tau (2 mg/mL, 500 μL) nanoparticle disperions at different pH.

Table 2. Estimated Thermodynamic Binding Parameters for the Interaction of γ-PGA-Tau with CS-*N*-Arg

	γ-PGA-Tau/CS-*N*-Arg			γ-PGA/CS
parameters	pH 6.0	pH 6.5	pH 7.4	pH 7.4
Stage I				
n	0.659	0.631	0.084	
K_a (M^{-1})	3.206×10^6	7.394×10^5	3.475×10^6	
ΔH (kJ mol^{-1})	495.6	322.1	−140.2	
ΔS (J mol^{-1} K^{-1})	1786	1192	−345.2	
Stage II				
n	0.665	0.644	0.352	0.017
K_a (M^{-1})	1.289×10^7	3.235×10^7	8.553×10^7	3.221×10^5
ΔH (kJ mol^{-1})	−209.7	−249.4	−194.2	1999
ΔS (J mol^{-1} K^{-1})	−567.2	−692.8	−499.7	6813

stage) was the critical point for the formation of colloidal complexes. The ITC analysis revealed that the critical point occurred near a γ-PGA-Tau to CS-*N*-Arg molar ratio of 0.63 ((C+T)/(A+G) charge ratio = 0.84). At pH 6.5, the ITC curve demonstrated a similar enthalpic binding signal, but the binding constant and binding enthalpy were slightly decreased (Figure 4B).

When CS-*N*-Arg was titrated with γ-PGA-Tau at pH 7.4, the enthalpic binding signal significantly changed. The ITC analysis showed that the γ-PGA-Tau/CS-*N*-Arg binding was exothermic, and the saturation shifted to smaller molar ratio (γ-PGA-Tau/CS-*N*-Arg molar ratio = 0.41) (Figure 4C). However, the exothermic binding enthalpy reached its maximum value at the very beginning of the γ-PGA/CS titration system (γ-PGA/CS molar ratio = 0.07) (Figure 5D). The quick saturation of binding sites reflected the weak γ-PGA/CS binding at this pH. In contrast, ITC analysis suggested that the binding sites of the CS-*N*-Arg/γ-PGA-Tau system were gradually saturated. The change of the enthalpic binding signal of the CS-*N*-Arg/γ-PGA-Tau system revealed that complex coacervation at pH 7.4 is more retainable because CS-*N*-Arg bears a larger number of positively

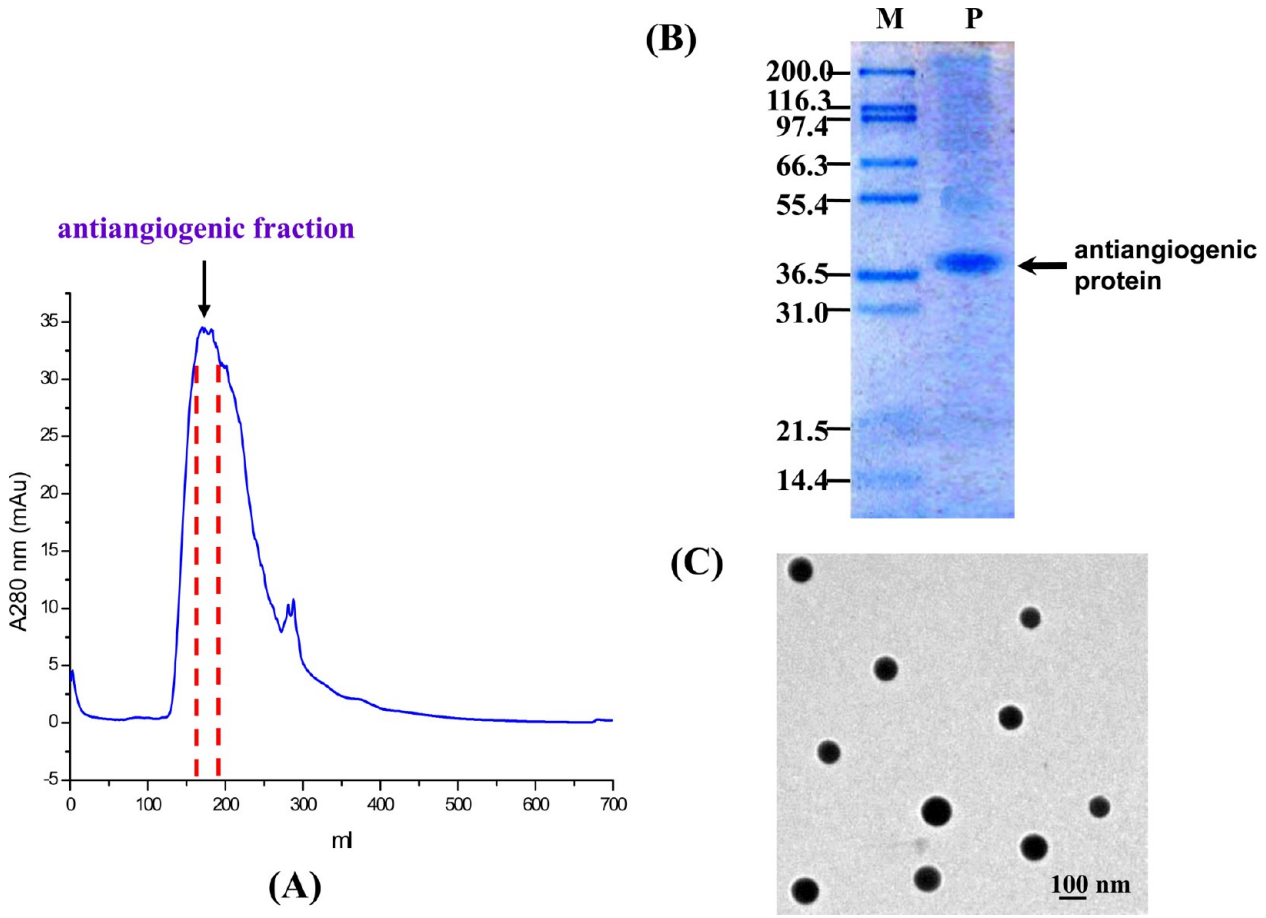

Figure 6. (A) Chromatography of the soluble fraction of anti-angiogenic protein from shark cartilage on Toyopearl HW-50 gel filtration column. (B) SDS-PAGE analysis of the purified anti-angiogenic protein. (C) TEM micrographs of protein-loaded γ-PGA-Tau/CS-*N*-Arg nanoparticles prepared at pH 6.0.

charged binding sites for intermolecular interactions. Estimated thermodynamic binding parameters are shown in Table 2.

FRET and Protein Release. In previous studies, fluorescent probes have been used to monitor the intracellular pH change in cancer cells[41] and oxidative stress in macrophage.[42] However, those nanoparticles were not used for protein loading and delivery. Figure 5A,B shows the γ-PGA-Tau/CS-*N*-Arg ratio-dependent and pH-responsive FRET spectra of the nanoparticle disperions prepared from CS-*N*-Arg and γ-PGA-Tau, respectively, conjugated with FITC and rhodamine B (Rhod B). The FRET efficiency was influenced by complexation/dissociation of CS-*N*-Arg/γ-PGA-Tau. In the titration study, the donor (FITC)-to-acceptor (Rhod B) fluorescence emission (ID/IA) in the spectra (excited with donor molecule excitation wavelength, 488 nm) decreased with the increase of the γ-PGA-Tau/CS-*N*-Arg molar ratio when aqueous Rhod B-γ-PGA-Tau (0−500 μL) was gradually added to aqueous FITC−CS-*N*-Arg at pH 6.0 (Figure 5A). This was due to the FRET effect arising from the complex coacervation subsequent to the formation of CS-*N*-Arg/γ-PGA-Tau polyion pairs, such that the fluorescence of the FITC moiety was quenched, while the emission intensity of Rhod-B increased because of a nonradiative transfer of energy from donor (FITC, 520 nm) to acceptor (Rhod-B, 585 nm).

Figure 5B shows the pH-dependent FRET spectra of FITC−CS-*N*-Arg/Rhod B-γ-PGA-Tau nanoparticle disperions. As pH increased, Rhod B emission decreased, while FITC emission increased because of a decrease in FRET from FITC to Rhod B. The decrease of the FRET efficiency at pH values higher than 6.5 was consistent with the above-mentioned pH-triggered dissociation of colloidal complex. Variation of the fluorescence intensity ratio can also be due to the pH-responsive properties of the fluorescent dyes conjugated with the polymers. Both effects contributed to the pH-sensitive characteristic of the nanoparticles. The ID/IA ratio increased from 0.058 to 1.557 as the pH value increased from 6.0 to 8.0 (27-fold higher than that measured at pH 6.0). FITC (donor)/Rhod B (acceptor) dual-emission-based fluorescence imaging was visualized by CLSM at various CS-*N*-Arg/γ-PGA-Tau molar ratios or different pH values (Figure 5C,D). By exciting the FITC−CS-*N*-Arg/Rhod B-γ-PGA-Tau nanoparticle dispersions with 488 ± 15 nm laser light, the fluorescence intensity of FITC (green emission) increased gradually, and the intensity of Rhod B fluorescence (red emission) decreased with increasing pH. The FITC−CS-*N*-Arg/Rhod B-γ-PGA-Tau nanoparticle disperion changes its fluorescent color from red (pH 6.0) to orange (pH 6.5) and then to green (pH 8.0). The results suggested that the fluorescent nanoparticles were able to detect alteration of the environmental acidity, especially for the pH in the intestinal tract (6.0−8.0). Moreover, the pH-responsive properties of CS-*N*-Arg/γ-PGA-Tau nanoparticles can be evaluated by monitoring the FITC/Rhod B emission ratios using a FRET microscopy method.

Anti-angiogenic protein extracted from shark cartilage was effectively purified during gel filtration chromatography (Figure 6A), and the final purified yields were approximately 100 mg.

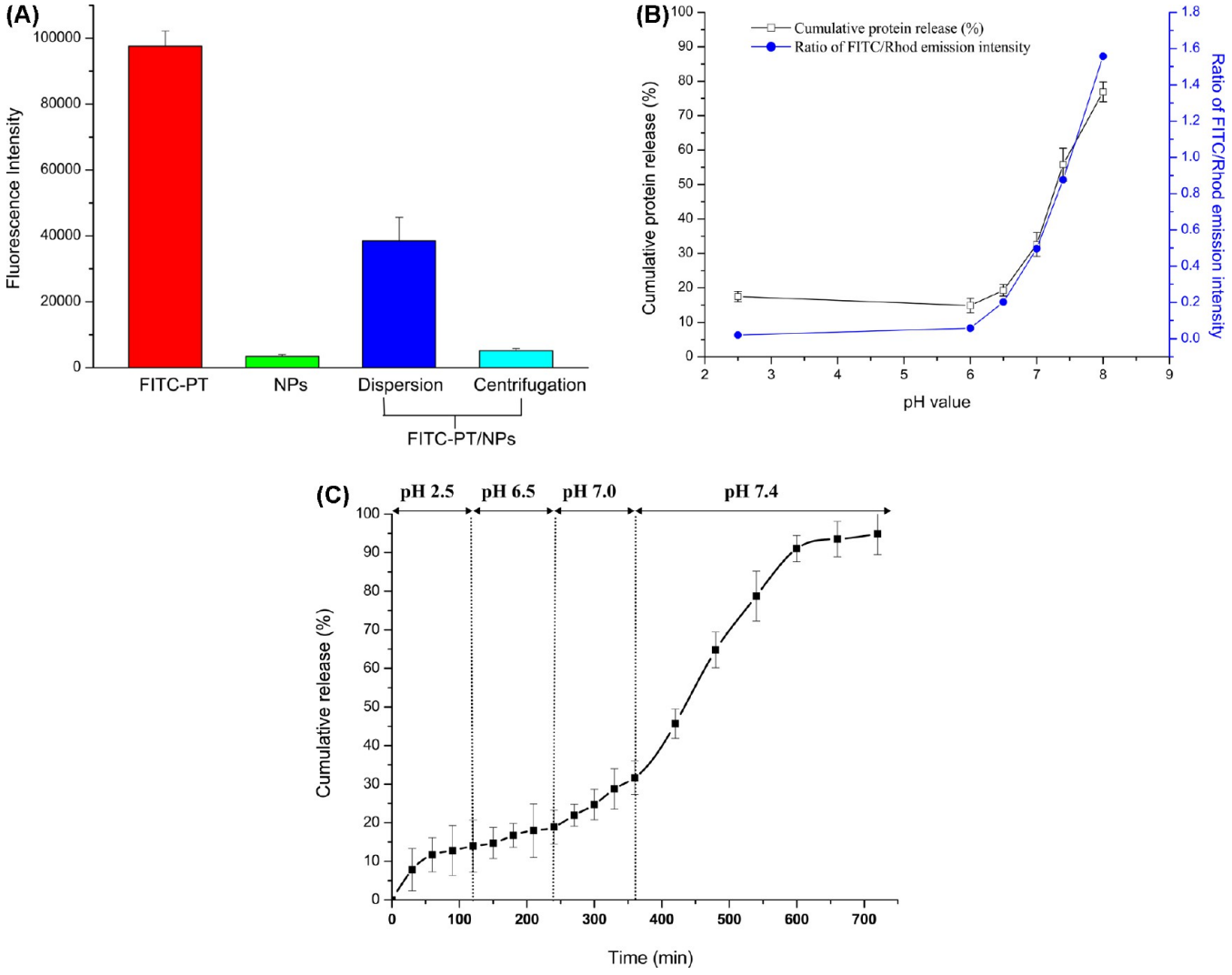

Figure 7. (A) Fluorescence intensity of FITC-labeled protein solution (FITC-PT, 25 μg/mL), protein-free (NPs), and protein-loaded (FITC-PT/NPs, 25 μg protein eq/mL) γ-PGA-Tau/CS-*N*-Arg nanoparticle dispersion. (B) Release of protein from CS-*N*-Arg/γ-PGA-Tau nanoparticles at pH 2.5, 6.0, 6.5, 7.0, 7.4, and 8.0, simulating the pH environments in the fasting stomach and the small intestine, respectively (n = 5 batches). (C) Time-dependent, continuous-release profiles of anti-angiogenic protein from the CS-*N*-Arg/γ-PGA-Tau NPs at pH 2.5, 6.5, 7.0, and 7.4 (n = 3 batches).

Analysis of the purified protein showed a single band by SDS-PAGE. Upon coomassie blue staining, a major band was observed in a position corresponding to a protein marker of about 38 kDa (Figure 6B). Transmission electron microscopy (TEM) micrographs indicated that the protein-loaded CS-*N*-Arg/γ-PGA-Tau nanoparticles prepared at pH 6.0 were spherical and intact (Figure 6C). Anti-angiogenic protein incorporated in the CS-*N*-Arg/γ-PGA-Tau nanoparticles were 38.6 $\pm$ 1.6% (loading efficiency) and 10.9 $\pm$ 0.8% (loading content), as compared with those of CS/γ-PGA NPs (32.8 $\pm$ 1.2% and 8.5 $\pm$ 0.6%). The isoelectric point (pI) of the purified anti-angiogenic protein is 7.6. By premixing anti-angiogenic protein with γ-PGA-Tau in water (pH 6.0), electrostatic attractions were formed between the positively charged protein and the negatively charged γ-PGA-Tau, thus improving the protein loading in subsequent prepared γ-PGA-Tau/CS-*N*-Arg nanocarriers. We also labeled the protein with FITC and determined fluorescence intensity of the protein-loaded nanoparticle dispersion (Figure 7A). The raw γ-PGA-Tau/CS-*N*-Arg nanoparticle demonstrated very weak fluorescence under 488 nm excitation. In contrast, the protein-loaded nanoparticle dispersion showed strong green fluorescence, which was comparable to the same equivalent of FITC-labeled protein. After centrifugation, fluorescence of the nanoparticle dispersion decreased, suggesting that the protein was distributed and located in the nanocarriers.

The pH-dependent release property of the nanoparticles was performed at distinct pH values over a period of 5 h (Figure 7B). CS-*N*-Arg/γ-PGA-Tau nanoparticles developed in this work was stable over a wide pH range (2.5−6.5); therefore, the release rate was slow in the pH range. In PBS (pH 7.4), a noticeable, increased release of anti-angiogenic protein from CS-*N*-Arg/γ-PGA-Tau nanoparticles was observed, and the release reached 55.8%. The increased release of protein in PBS was due to the deprotonation of most primary amines of chitosan in the CS-Arg conjugates as pH was higher than 7.0. Figure 7C shows the time-dependent, continuous-release profiles of anti-angiogenic protein from the CS-*N*-Arg/γ-PGA-Tau NPs at pH 2.5, 6.5, 7.0, and 7.4, simulating the pH change of gastrointestinal (GI) tract. The protein release rates were slow at pH 2.5 (120 min) and 6.5 (120 min) but were fast at pH 7.0 (120 min) and 7.4 (360 min). The results of the time-dependent release profiles

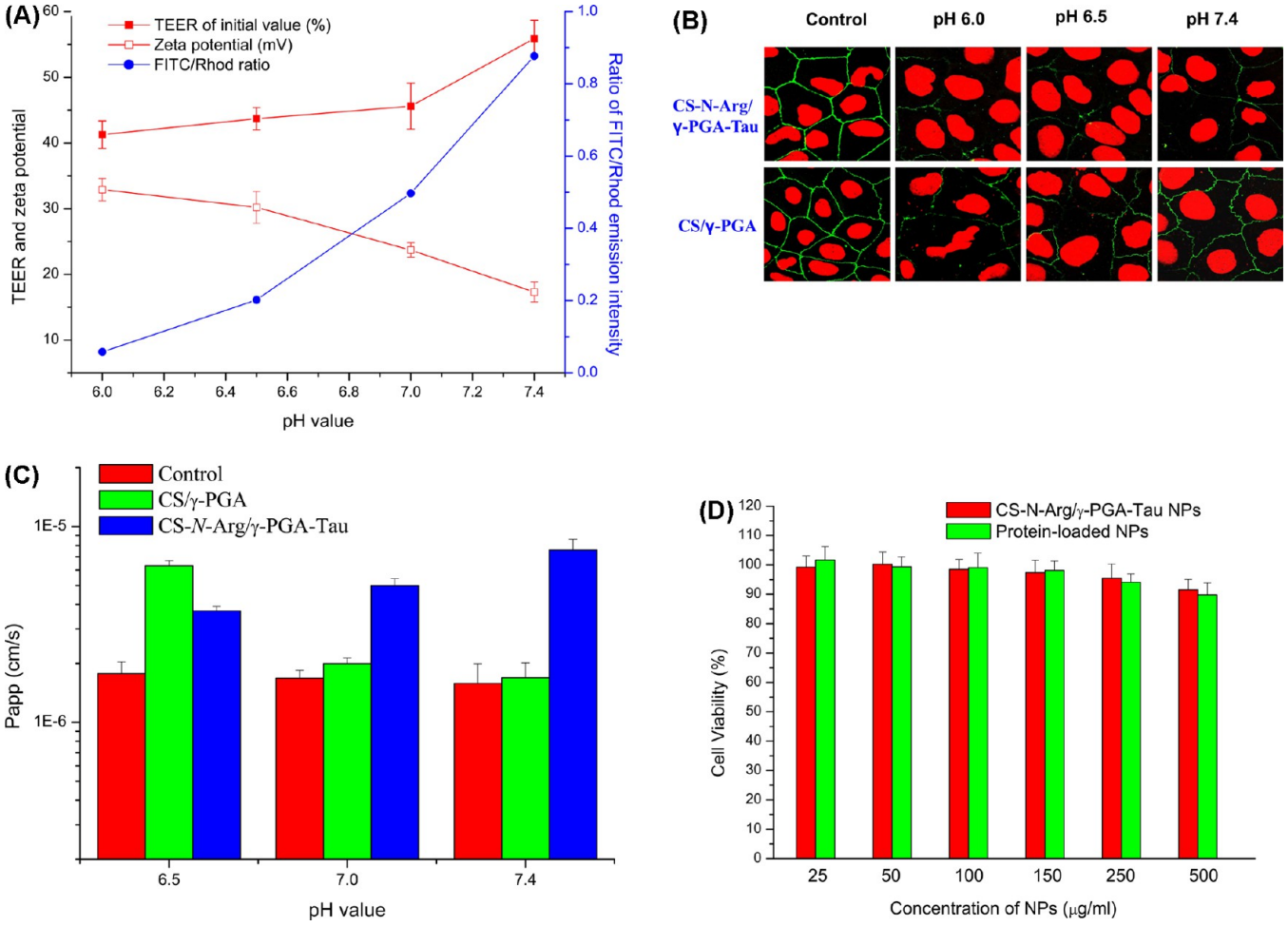

Figure 8. (A) Effects of CS-*N*-Arg/γ-PGA-Tau nanoparticles on TEER values of Caco-2 cell monolayers at distinct pH values (n = 5 batches). (B) Fluorescence images of Caco-2 cell monolayers immunofluorescently stained for ZO-1 protein and PI after incubation with nanoparticles for 120 min. (C) The P_{app} values of anti-angiogenic protein transported by the CS/γ-PGA and CS-*N*-Arg/γ-PGA-Tau nanoparticles at distinct pH values (n = 5 batches). (D) The dose-dependent (25−500 μg/mL) cytotoxicity effects on Caco-2 cell induced by protein-free and the protein-loaded nanoparticles (n = 5 batches).

suggested that anti-angiogenic protein was released from the nanoparticles in a pH-dependent manner.

The protein release property could be correlated to the above-mentioned pH-responsive dual-emission effect. As shown in Figure 5B, at pH lower than 6.0, ratio of donor/acceptor emission intensity was still very low (FITC/Rhod = 0.058). However, the ID/IA ratio increased from 0.058 to 0.877 as the pH value increased from 6.0 to 7.4. At pH 8.0, the ratio of FITC/Rhod emission intensity even increased to 1.557, which was approximately 27-fold higher than the emission ratio measured at pH 6.0. The significant increase of the ratio of FITC/Rhod emission intensity is due to the decrease of the FRET efficiency at this pH value and can be correlated to the increase of protein release ratio (76.9%).

TEER and Protein Transport. Subsequent to the dissociation, anti-angiogenic protein could release from the nanoparticles at a quicker rate. Therefore, the protein release at different pH regions in the intestinal environments can be monitored from the ratio of FITC/Rhod emission intensity of the nanoparticles via modulating the pH-responsive dual-emission process. Caco-2 cell is traditionally used for permeability testing and predicting drug absorption.[43] Tight junction opening triggered by nanoparticles leads to the transport of protein across Caco-2 cell monolayers, which are dependent on the environmental pH.[44] As shown in Figure 8A, at pH 7.0 and 7.4, CS-*N*-Arg/γ-PGA-Tau nanoparticles were still able to cause a considerable reduction in TEER (45.6 ± 3.5% and 55.9 ± 2.8% of the initial values) because 37.6% and 29.1% of the theoretical positive charges remained on CS-*N*-Arg macromolecular chains (the ζ potentials were 23.7 and 17.3 mV). The green fluorescence indicated ZO-1 protein, whereas the red fluorescence was from the nuclei staining dye (PI). The staining for ZO-1 proteins appeared as discontinuous rings in Caco-2 cell (Figure 8B), revealing that the nanoparticles were able to mediate the opening of tight junctions. The reduction in TEER at different pH regions in the intestinal environments can be correlated to the change in ratio of FITC/Rhod emission intensity of the nanoparticles. As the ratio of FITC/Rhod emission intensity increased, the ζ potential of the nanoparticles decreased, whereas the percentage TEER (%) of initial values increased (Figure 8A). At pH 7.4, less positive charge (A+G = 29.1%) was retained by CS-*N*-Arg as compared to the charge retained at pH 6.0 (A+G = 71.2%), 6.5 (A+G = 54.4%), and 7.0 (A+G = 37.6%). The ζ potential decreased to 17.3 mV. The CS-*N*-Arg/γ-PGA-Tau complex was partially dissociated; therefore, the ID/IA ratio significantly increased (FITC/Rhod = 0.877) as pH increased to 7.4, which was approximately 15-fold higher than the emission ratio measured at pH 6.0. The decreases in ζ

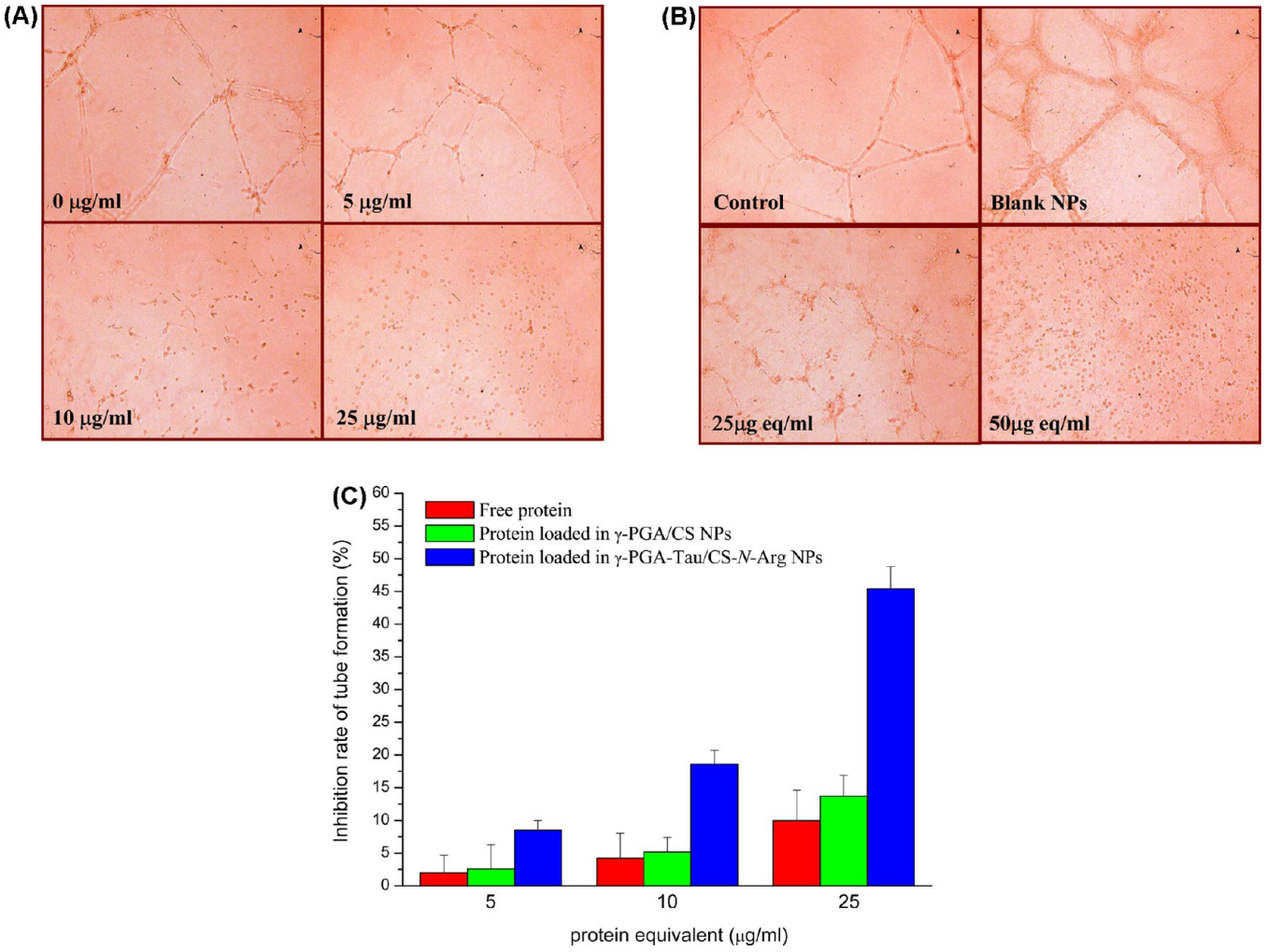

Figure 9. (A) Inhibition of HUVEC tube formation by directly treating HUVEC with 5−25 μg/mL of anti-angiogenic protein. (B) Inhibition of HUVEC tube formation by adding free protein, protein-free nanoparticles and protein-loaded CS-*N*-Arg/γ-PGA-Tau nanoparticles (25 and 50 μg anti-angiogenic protein eq/mL) to the apical compartment (pH 7.4) with HUVEC cultured in the receiving plates. (C) Inhibition rate of tube length of HUVECs measured on Matrigel, by adding free protein and protein-loaded nanoparticles (5, 10, and 25 μg anti-angiogenic protein eq/mL) to the apical compartment (pH 7.4) with HUVEC cultured in the receiving plates (n = 5 batches).

potential and increases in TEER (revealing the opening of TJ) with the increases of pH values were indicated by the change in color of the fluorescence image from red to green due to increasing the ratio of donor/acceptor emission intensity (Figure 5D).

Nanoparticles mediate the opening of TJ and can result in an improvement in paracellular transport of anti-angiogenic protein compared to those transported without nanoparticles. The surface charge of nanoparticles and the pH value have significant effects on the apparent permeability coefficient (P_{app}). The P_{app} values of anti-angiogenic protein transported by the CS/γ-PGA and CS-*N*-Arg/γ-PGA-Tau nanoparticles at pH 6.5 were 3.6 and 2.1 folds higher than that of free protein (Figure 8C). However, as pH increases to 7.4, the P_{app} values of protein-loaded CS/γ-PGA nanoparticles were close to the free protein (1.1-fold). The P_{app} value of protein-loaded CS-*N*-Arg/γ-PGA-Tau nanoparticles was 4.8-fold greater than its free protein counterpart. At this pH value, CS-*N*-Arg/γ-PGA-Tau nanoparticles still retained enough positive charges on the surface, thereby affecting the dislocation of TJ-associated protein (ZO-1), closely related to the permeation-enhancing effect. The sulfonate groups on γ-PGA-Tau also contributed to the opening of TJ due to their Ca^{2+} ion binding affinity, leading to the increased transport of protein. Moreover, CS-*N*-Arg/γ-PGA-Tau nanoparticles released protein at a faster rate at pH 7.4 than pH 6.0 and 7.0. These factors contributed to enhance permeation of proteins through the Caco-2 monolayer. Figure 8D shows the dose-dependent cytotoxicity effects on Caco-2 cell induced by protein-free and the protein-loaded nanoparticles. The results indicate that the nanoparticles induce very low cytotoxicity in the range of 25−500 μg/mL as measured by the MTT assay.

Inhibition of HUVECs Tube Formation. In the controlled inhibitory experiment, an amount of anti-angiogenic protein (without nanoparticles) was directly added into 24-well plates after seeding HUVECs onto vascular endothelial growth factor (VEGF)-containing Matrigel; subsequently, cellular morphology was observed. Figure 9A shows the inhibiton efficiency of anti-angiogenic protein (5−25 μg/mL) on capillary tube formation at 24 h post treatment. Anti-angiogenic protein disrupted capillary tube formation on Matrigel at a low concentration of 10 μg/mL. The anti-angiogenic protein effectively competed against the binding of VEGF, which has been proven to be involved in tumor growth and metastasis.[20]

Anti-angiogenic protein transported across Caco-2 cells via nanoparticles was compared with free protein for the inhibition of capillary tube formation. Original anti-angiogenic protein and blank nanoparticles were not able to inhibit HUVECs tube formation in the basal compartment. However, anti-angiogenic protein transported from the apical compartment to the receiving plates (cultured with HUVECs) using protein-loaded CS-*N*-Arg/γ-PGA-Tau nanoparticles exhibited significant dose-dependent tubulogenesis inhibition activity. CS-*N*-Arg/γ-PGA-Tau nanoparticles at 50 μg of anti-angiogenic protein equivalent per milliliter almost completely inhibited tube formation of HUVECs (Figure 9B). As the anti-angiogenic protein was difficult to permeate across the barrier of Caco-2 cell monolayer, HUVECs were poorly inhibited by the free protein. Moreover, the protein transported by CS/γ-PGA nanoparticles (5, 10, and 25 μg protein eq/mL) are less effective in the inhibition of HUVECs tube formation as compared to those transported by CS-*N*-Arg/γ-PGA-Tau nanoparticles at the same protein equivalent ($P < 0.05$) (Figure 9C). Extent of inhibition was dependent on the amount of anti-angiogenic protein added to the apical side of the cell monolayer as well as the protein release and transport across Caco-2 cell monolayers. The protein-loaded CS-*N*-Arg/γ-PGA-Tau nanoparticles were 4.5-fold more potent than their free protein counterparts in the inhibition of HUVECs tube formation. The data reveal that the CS-*N*-Arg/γ-PGA-Tau nanoparticles facilitate the transport of anti-angiogenic protein across Caco-2 monolayer, and the anti-angiogenic activity of the transported protein is retained.

CONCLUSIONS

A FRET-based dual-emission and pH-responsive nanocarrier has been developed based on the assembly of two oppositely charged polyions, namely, CS-*N*-Arg and γ-PGA-Tau. The nanocarrier modulated the intensity of the emission from donor and acceptor fluorophores and triggered the opening of intestinal epithelial TJ at different levels in response to pH changes. The ID/IA ratio was altered in response to pH changes of intestinal environmental (pH 6.0−8.0) and was correlated to the release of protein from nanoparticles and the decrease in transepithelial electrical resistance (TEER). The nanoparticles facilitated the transport of anti-angiogenic protein across Caco-2 monolayer, while the transported anti-angiogenic protein retained the activity and could effectively inhibit the HUVECs tube formation.

AUTHOR INFORMATION

Corresponding Authors

*E-mail: hwsung@mx.nthu.edu.tw. (H.W.S.)
*E-mail: flmi530326@tmu.edu.tw. Fax: 886-2-2735-6689. (F.L.M.)

Author Contributions

[¶]The contributions by the two collaborating parties are equal.

Notes

The authors declare no competing financial interest.

ACKNOWLEDGMENTS

This work was supported by Grant No. NSC 102-2120-M-007-008-CC1 from the National Science Council, Taiwan, ROC.

REFERENCES

(1) Carmeliet, P. Angiogenesis in Life, Disease and Medicine. *Nature* **2005**, *438*, 932−936.
(2) Bremer, C.; Tung, C. H.; Weissleder, R. In Vivo Molecular Target Assessment of Matrix Metalloproteinase Inhibition. *Nat. Med.* **2001**, *7*, 743−748.
(3) Yancopoulos, G. D.; Davis, S.; Gale, N. W.; Rudge, J. S.; Wiegand, S. J.; Holash, J. Vascular-Specific Growth Factors and Blood Vessel Formation. *Nature* **2000**, *407*, 242−248.
(4) Skandalis, S. S.; Gialeli, C.; Theocharis, A. D.; Karamanos, N. K. Advantages of Nanomedicine in The Pharmacological Targeting of Hyaluronan-CD44 Interactions and Signaling in Cancer. *Adv. Cancer Res.* **2014**, *123*, 277−317.
(5) Yim, H.; Park, S. J.; Bae, Y. H.; Na, K. Biodegradable Cationic Nanoparticles Loaded with An Anticancer Drug for Deep Penetration of Heterogeneous Tumours. *Biomaterials* **2013**, *34*, 7674−7682.
(6) Duan, X.; Wang, P.; Men, K.; Gao, X.; Huang, M.; Gou, M.; Chen, L.; Qian, Z.; Wei, Y. Treating Colon Cancer with A Suicide Gene Delivered by Self-assembled Cationic MPEG-PCL Micelles. *Nanoscale* **2012**, *4*, 2400−2407.
(7) Deng, Z. J.; Morton, S. W.; Ben-Akiva, E.; Dreaden, E. C.; Shopsowitz, K. E.; Hammond, P. T. Layer-by-Layer Nanoparticles for Systemic Codelivery of An Anticancer Drug and siRNA for Potential Triple-Negative Breast Cancer Treatment. *ACS Nano* **2013**, *7*, 9571−9584.
(8) Kanwar, J. R.; Mahidhara, G.; Kanwar, R. K. Antiangiogenic Therapy using Nanotechnological-Based Delivery System. *Drug Discovery Today* **2011**, *16*, 188−202.
(9) El-Dakdouki, M. H.; Xia, J.; Zhu, D. C.; Kavunja, H.; Grieshaber, J.; O'Reilly, S.; McCormick, J. J.; Huang, X. Assessing The In Vivo Efficacy of Doxorubicin Loaded Hyaluronan Nanoparticles. *ACS Appl. Mater. Interfaces* **2014**, *6*, 697−705.
(10) Jia, M.; Li, Y.; Yang, X.; Huang, Y.; Wu, H.; Huang, Y.; Lin, J.; Li, Y.; Hou, Z.; Zhang, Q. Methotrexate and Mitomycin C Loaded Pegylated Chitosan Nanoparticles for Targeted Drug Codelivery and Synergistic Anticancer Effect. *ACS Appl. Mater. Interfaces* **2014**, *6*, 11413−11423.
(11) Xie, Y.; Qiao, H.; Su, Z.; Chen, M.; Ping, Q.; Sun, M. PEGylated Carboxymethyl Chitosan/Calcium Phosphate Hybrid Anionic Nanoparticles Mediated hTERT siRNA Delivery for Anticancer Therapy. *Biomaterials* **2014**, *35*, 7978−7991.
(12) Vivek, R.; Thangam, R.; NipunBabu, V.; Rejeeth, C.; Sivasubramanian, S.; Gunasekaran, P.; Muthuchelian, K.; Kannan, S. Multifunctional HER2-Antibody Conjugated Polymeric Nanocarrier-Based Drug Delivery System for Multi-Drug-Resistant Breast Cancer Therapy. *ACS Appl. Mater. Interfaces* **2014**, *6*, 6469−6480.
(13) He, Q.; Shi, J. MSN Anticancer Nanomedicines: Chemotherapy Enhancement, Overcoming of Drug Resistance, and Metastasis Inhibition. *Adv. Mater.* **2014**, *26*, 391−411.
(14) Lee, D. Y.; Kim, S. K.; Kim, Y. S.; Son, D. H.; Nam, J. H.; Kim, I. S.; Park, R. W.; Kim, S. Y.; Byun, Y. Suppression of Angiogenesis and Tumor Growth by Orally Active Deoxycholic Acid-Heparin Conjugate. *J. Controlled Release* **2007**, *118*, 310−317.
(15) Park, J. W.; Jeon, O. C.; Kim, S. K.; Al-Hilal, T. A.; Jin, S. J.; Moon, H. T.; Yang, V. C.; Kim, S. Y.; Byun, Y. High Antiangiogenic and Low Anticoagulant Efficacy of Orally Active Low Molecular Weight Heparin Derivatives. *J. Controlled Release* **2010**, *148*, 317−326.
(16) Benny, O.; Fainaru, O.; Adini, A.; Cassiola, F.; Bazinet, L.; Adini, I.; Pravda, E.; Nahmias, Y.; Koirala, S.; Corfas, G.; D'Amato, R. J.; Folkman, J. An Orally Delivered Small-Molecule Formulation with Antiangiogenic and Anticancer Activity. *Nat. Biotechnol.* **2008**, *26*, 799−807.
(17) Satchi-Fainaro, R.; Puder, M.; Davies, J. W.; Tran, H. T.; Sampson, D. A.; Greene, A. K.; Corfas, G.; Folkman, J. Targeting Angiogenesis with A Conjugate of HPMA Copolymer and TNP-470. *Nat. Med.* **2004**, *10*, 255−261.
(18) Lee, A.; Langer, R. Shark Cartilage Contains Inhibitors of Tumor Angiogenesis. *Science* **1983**, *221*, 1185−1187.
(19) Boivin, D.; Gendron, S.; Beaulieu, E.; Gingras, D.; Beliveau, R. The Antiangiogenic Agent Neovastat (AE-941) Induces Endothelial Cell Apoptosis. *Mol. Cancer Ther.* **2002**, *1*, 795−802.

(20) Beliveau, R.; Gingras, D.; Kruger, E. A.; Lamy, S.; Sirois, P.; Simard, B.; Sirois, M. G.; Tranqui, L.; Baffert, F.; Beaulieu, E.; Dimitriadou, V.; Pepin, M. C.; Courjal, F.; Ricard, I.; Poyet, P.; Falardeau, P.; Figg, W. D.; Dupont, E. The Antiangiogenic Agent Neovastat (AE-941) Inhibits Vascular Endothelial Growth Factor-Mediated Biological Effects. *Clin. Cancer Res.* **2002**, *8*, 1242−1250.
(21) Lu, C.; Lee, J. J.; Komaki, R.; Herbst, R. S.; Feng, L.; Evans, W. K.; Choy, H.; Desjardins, P.; Esparaz, B. T.; Truong, M. T.; Saxman, S.; Kelaghan, J.; Bleyer, A.; Fisch, M. J. Chemoradiotherapy with or without AE-941 In Stage III Non-small Cell Lung Cancer: A Randomized Phase III Trial. *J. Natl. Cancer Inst.* **2010**, *102*, 859−865.
(22) Chen, J.; Ouyang, J.; Kong, J.; Zhong, W.; Xing, M. M. Photo-Cross-Linked and pH-Sensitive Biodegradable Micelles for Doxorubicin Delivery. *ACS Appl. Mater. Interfaces* **2013**, *5*, 3108−3117.
(23) Binauld, S.; Stenzel, M. H. Acid-Degradable Polymers for Drug Delivery: a Decade of Innovation. *Chem. Commun.* **2013**, *49*, 2082−2102.
(24) Xia, B.; Wang, X.; He, F.; Cui, Q.; Li, L. Self-Assembly of Conjugated Polymer on Hybrid Nanospheres for Cellular Imaging Applications. *ACS Appl. Mater. Interfaces* **2012**, *4*, 6332−6337.
(25) Banerjee, A.; Bhatia, D.; Saminathan, A.; Chakraborty, S.; Kar, S.; Krishnan, Y. Controlled Release of Encapsulated Cargo from A DNA Icosahedron using A Chemical Trigger. *Angew. Chem., Int. Ed.* **2013**, *52*, 6854−6857.
(26) Chen, W.; Meng, F.; Cheng, R.; Zhong, Z. pH-Sensitive Degradable Polymersomes for Triggered Release of Anticancer Drugs: A Comparative Study with Micelles. *J. Controlled Release* **2010**, *142*, 40−46.
(27) Feng, W.; Nie, W.; He, C.; Zhou, X.; Chen, L.; Qiu, K.; Wang, W.; Yin, Z. Effect of pH-Responsive Alginate/Chitosan Multilayers Coating on Delivery Efficiency, Cellular Uptake and Biodistribution of Mesoporous Silica Nanoparticles Based Nanocarriers. *ACS Appl. Mater. Interfaces* **2014**, *6*, 8447−8460.
(28) Wang, S.; Zhang, S.; Liu, J.; Liu, Z.; Su, L.; Wang, H.; Chang, J. pH- and Reduction-Responsive Polymeric Lipid Vesicles for Enhanced Tumor Cellular Internalization and Triggered Drug Release. *ACS Appl. Mater. Interfaces* **2014**, *6*, 10706−10713.
(29) Hu, X.; Neoh, K. G.; Shi, Z.; Kang, E. T.; Poh, C.; Wang, W. An In Vitro Assessment of Titanium Functionalized with Polysaccharides Conjugated with Vascular Endothelial Growth Factor for Enhanced Osseointegration and Inhibition of Bacterial Adhesion. *Biomaterials* **2010**, *31*, 8854−8863.
(30) Sonaje, K.; Lin, K. J.; Wang, J. J.; Mi, F. L.; Chen, C. T.; Juang, J. H.; Sung, H. W. Self-Assembled pH-Sensitive Nanoparticles: A Platform for Oral Delivery of Protein Drugs. *Adv. Funct Mater.* **2010**, *20*, 3695−3700.
(31) Ho, Y. C.; Liao, Z. X.; Panda, N.; Tang, D. W.; Yu, S. H.; Mi, F. L.; Sung, H. W. Self-Organized Nanoparticles Prepared by Guanidine- and Disulfide-Modified Chitosan as A Gene Delivery Carrier. *J. Mater. Chem.* **2011**, *21*, 16918−16927.
(32) Sun, L.; Wang, Y.; Jiang, T.; Zheng, X.; Zhang, J.; Sun, J.; Sun, C.; Wang, S. Novel Chitosan-Functionalized Spherical Nanosilica Matrix as An Oral Sustained Drug Delivery System for Poorly Water-Soluble Drug Carvedilol. *ACS Appl. Mater. Interfaces* **2013**, *5*, 103−113.
(33) Hsu, L. W.; Ho, Y. C.; Chuang, E. Y.; Chen, C. T.; Juang, J. H.; Su, F. Y.; Hwang, S. M.; Sung, H. W. Effects of pH on Molecular Mechanisms of Chitosan-Integrin Interactions and Resulting Tight-Junction Disruptions. *Biomaterials* **2013**, *34*, 784−793.
(34) Yu, S. H.; Tang, D. W.; Hsieh, H. Y.; Wu, W. S.; Lin, B. X.; Chuang, E. Y.; Sung, H. W.; Mi, F. L. Nanoparticle-Induced Tight-Junction Opening for The Transport of An Anti-Angiogenic Sulfated Polysaccharide Across Caco-2 Cell Monolayers. *Acta. Biomater.* **2013**, *9*, 7449−7459.
(35) Chuang, E. Y.; Nguyen, G.. T.; Su, F. Y.; Lin, K. J.; Chen, C. T.; Mi, F. L.; Yen, T. C.; Juang, J. H.; Sung, H. W. Combination Therapy via Oral Co-Administration of Insulin- and Exendin-4-Loaded Nanoparticles to Treat Type 2 Diabetic Rats Undergoing OGTT. *Biomaterials* **2013**, *34*, 7994−8001.
(36) Lee, A.; Langer, R. Shark Cartilage Contains Inhibitors of Tumor Angiogenesis. *Science* **1983**, *221*, 1185−1187.
(37) Zhang, X.; Li, J.; Li, W.; Zhang, A. Synthesis and Characterization of Thermo- and pH-Responsive Double-Hydrophilic Diblock Copolypeptides. *Biomacromolecules* **2007**, *8*, 3557−3567.
(38) Tang, D. W.; Yu, S. H.; Ho, Y. C.; Mi, F. L.; Kuo, P. L.; Sung, H. W. Heparinized Chitosan/Poly(gamma-glutamic acid) Nanoparticles for Multi-Functional Delivery of Fibroblast Growth Factor and Heparin. *Biomaterials* **2010**, *31*, 9320−9332.
(39) Lin, I. C.; Liang, M.; Liu, T. Y.; Ziora, Z. M.; Monteiro, M. J.; Toth, I. Interaction of Densely Polymer-Coated Gold Nanoparticles with Epithelial Caco-2 Monolayers. *Biomacromolecules* **2011**, *12*, 1339−1348.
(40) Huang, Y.; Lapitsky, Y. Determining The Colloidal Behavior of Ionically Cross-Linked Polyelectrolytes with Isothermal Titration Calorimetry. *J. Phys. Chem. B* **2013**, *117*, 9548−9557.
(41) Chiu, Y. L.; Chen, S. A.; Chen, J. H.; Chen, K. J.; Chen, H. L.; Sung, H. W. A Dual-Emission Forster Resonance Energy Transfer Nanoprobe for Sensing/Imaging pH Changes In The Biological Environment. *ACS Nano* **2010**, *4*, 7467−7474.
(42) Pu, H. L.; Chiang, W. L.; Maiti, B.; Liao, Z. X.; Ho, Y. C.; Shim, M. S.; Chuang, E. Y.; Xia, Y.; Sung, H. W. Nanoparticles with Dual Responses to Oxidative Stress and Reduced pH for Drug Release and Anti-Inflammatory Applications. *ACS Nano* **2014**, *8*, 1213−1221.
(43) Artursson, P.; Palm, K.; Luthman, K. Caco-2 Monolayers In Experimental and Theoretical Predictions of Drug Transport. *Adv. Drug Delivery Rev.* **2012**, *64*, 280−289.
(44) Chen, M. C.; Mi, F. L.; Liao, Z. X.; Hsiao, C. W.; Sonaje, K.; Chung, M. F.; Hsu, L. W.; Sung, H. W. Recent Advances in Chitosan-Based Nanoparticles for Oral Delivery of Macromolecules. *Adv. Drug Delivery Rev.* **2013**, *65*, 865−879.